Siberian and temperate ecosystems shape Northern Hemisphere atmospheric CO2 seasonal amplification

Xin Lin, Brendan M. Rogers, Colm O. Sweeney, Frédéric Chevallier, Mikhail Yu Arshinov, Edward J. Dlugokencky, Toshinobu Machida, Motoki Sasakawa, Pieter P. Tans, Gretchen Keppel-Aleks

Siberian and temperate ecosystems shape Northern Hemisphere atmospheric CO_2 seasonal amplification

Xin Lin[a,1], Brendan M. Rogers[b], Colm Sweeney[c], Frédéric Chevallier[d], Mikhail Arshinov[e], Edward Dlugokencky[c], Toshinobu Machida[f], Motoki Sasakawa[f], Pieter Tans[c], and Gretchen Keppel-Aleks[a,1]

[a]Climate and Space Sciences and Engineering, University of Michigan, Ann Arbor, MI 48109; [b]Woods Hole Research Center, Falmouth, MA 02540; [c]Global Monitoring Laboratory, National Oceanic and Atmospheric Administration, Boulder, CO 80305; [d]Laboratoire des Sciences du Climat et de l'Environnement/Institut Pierre Simon Laplace, Commissariat à l'Énergie Atomique et aux Énergies Alternatives–CNRS–Université de Versailles Saint-Quentin-en-Yvelines, Université Paris-Saclay, F-91191 Gif-sur-Yvette, France; [e]Vladimir Evseevich Zuev Institute of Atmospheric Optics, Siberian Branch, Russian Academy of Sciences, Tomsk 634055, Russia; and [f]Center for Global Environmental Research, National Institute for Environmental Studies, Tsukuba, Ibaraki 305-8506, Japan

Edited by Christopher B. Field, Stanford University, Stanford, CA, and approved July 10, 2020 (received for review August 16, 2019)

The amplitude of the atmospheric CO_2 seasonal cycle has increased by 30 to 50% in the Northern Hemisphere (NH) since the 1960s, suggesting widespread ecological changes in the northern extratropics. However, substantial uncertainty remains in the continental and regional drivers of this prominent amplitude increase. Here we present a quantitative regional attribution of CO_2 seasonal amplification over the past 4 decades, using a tagged atmospheric transport model prescribed with observationally constrained fluxes. We find that seasonal flux changes in Siberian and temperate ecosystems together shape the observed amplitude increases in the NH. At the surface of northern high latitudes, enhanced seasonal carbon exchange in Siberia is the dominant contributor (followed by temperate ecosystems). Arctic-boreal North America shows much smaller changes in flux seasonality and has only localized impacts. These continental contrasts, based on an atmospheric approach, corroborate heterogeneous vegetation greening and browning trends from field and remote-sensing observations, providing independent evidence for regionally divergent ecological responses and carbon dynamics to global change drivers. Over surface midlatitudes and throughout the midtroposphere, increased seasonal carbon exchange in temperate ecosystems is the dominant contributor to CO_2 amplification, albeit with considerable contributions from Siberia. Representing the mechanisms that control the high-latitude asymmetry in flux amplification found in this study should be an important goal for mechanistic land surface models moving forward.

carbon dioxide | seasonal cycle | amplification | Arctic-boreal | global change

The seasonal oscillation of atmospheric CO_2 is mainly driven by the balance between seasonal land carbon uptake via photosynthesis and release via respiration and disturbances (1), and the amplitude of this annual cycle characterizes the intensity of the seasonal net carbon exchange (NEE) between the land and atmosphere. Ground-based and airborne CO_2 measurements since the 1960s show an increase in the seasonal cycle amplitude (SCA) in the Northern Hemisphere (NH) high latitudes by 30 to 50% (2, 3), suggesting widespread ecological changes in the northern extratropics (2–4). However, the regions and underlying processes driving this trend are still poorly understood. Previous studies based on atmospheric measurements and models disagree on whether flux changes in boreal or temperate ecosystems dominate the observed SCA enhancement (3, 5). Meanwhile, simulations of atmospheric CO_2 driven by land fluxes from state-of-the-art land surface models (LSMs) generally underestimate the amplitude increase (3, 6), and analyses from factorial LSM experiments do not agree on whether climate change, CO_2 fertilization, or land use change provide the driving mechanism (7–12).

Although the CO_2 SCA has increased across most NH sampling sites (3, 7, 10), substantial variability in the magnitude of the trends from site to site suggests heterogeneity in regional flux signatures. Spatial variability in ecosystem trends is likewise supported by ecological observations, which suggest distinct regional responses to global change drivers. For example, increasing vegetation productivity has been observed across large portions of the circumpolar zone, but drought and disturbances such as pests and wildfire have decreased productivity over extensive areas in boreal North America (13–15). The spatially nonuniform changes in climate drivers and ecosystem responses, propagated by atmospheric transport, complicate interpretation of the atmospheric amplification signals and attribution of driving mechanisms. It is therefore important to disentangle the regional imprints that these ecological changes leave on the carbon cycle, including identifying the dominant contributing regions to SCA trends (i.e., where global change factors are accelerating the carbon cycle) and areas with negligible influence (i.e., where global change factors either are having a negligible

Significance

The increasing atmospheric CO_2 seasonal cycle amplitude in the Northern Hemisphere suggests northern ecosystems are responding strongly to global change. Considerable uncertainties remain regarding drivers of these changes and their locations. We find that seasonal flux changes in Siberian and temperate ecosystems together shape the increasing CO_2 amplitude. Particularly, enhanced seasonal carbon exchange in Siberia drives most of observed amplitude increases at the surface of northern high latitudes. Arctic-boreal North America shows much smaller changes in flux seasonality and has only localized impacts, consistent with more browning in this region from field and satellite observations. Our findings highlight divergent ecosystem responses among regions, countering the simple narrative that CO_2 fertilization and climate warming are the dominant drivers.

Author contributions: X.L., B.M.R., and G.K.-A. designed research; X.L. performed research; X.L. analyzed data; C.S. provided aircraft measurements from NOAA's Global Greenhouse Gas Reference Network (GGGRN); F.C. developed the Copernicus Atmosphere Monitoring Service CO_2 inversion datasets and contributed to the interpretation of inversions; M.A. and M.S. provided National Institute for Environmental Studies/Center for Global Environmental Research tall tower and aircraft measurements in Siberia; E.D. and P.T. provided surface measurements from NOAA's GGGRN; T.M. provided aircraft measurements from the Comprehensive Observation Network for TRace gases by AIrLiner (CONTRAIL) project; and X.L., B.M.R., C.S., F.C., M.A., E.D., T.M., M.S., P.T., and G.K.-A. wrote the paper.

The authors declare no competing interest.

This article is a PNAS Direct Submission.

[1]To whom correspondence may be addressed. Email: xinlinn@umich.edu or gkeppela@umich.edu.

This article contains supporting information online at https://www.pnas.org/lookup/suppl/doi:10.1073/pnas.1914135117/-/DCSupplemental.

First published August 17, 2020.

effect on seasonal CO_2 fluxes or are counteracting each other through positive and negative effects).

In this study, we present a regional attribution of CO_2 seasonal amplification in the NH over the past 4 decades. We accomplished this using a tagged atmospheric transport model, which has proven to be a useful tool to partition contributions of individual ecosystems or flux components to the mean SCA and its changes (1, 3, 4, 7, 10, 16). In contrast to previous studies that typically prescribed fluxes from data-driven or mechanistic LSMs, we instead used fluxes constrained by atmospheric CO_2 measurements. Compared to bottom-up flux estimates, these optimized fluxes from top-down approaches should be more realistic in terms of their spatial and temporal variations and able to reproduce changes in atmospheric CO_2, including the increasing trend in SCA. We used these fluxes in a forward modeling framework; evaluated the resulting SCA patterns using a diverse set of atmospheric CO_2 observations from surface, tower, and aircraft platforms; and quantified regional contributions to SCA trends at sites with long-standing CO_2 observations and across the entire NH.

Materials and Methods

Tagged CO_2 Transport Simulations. Goddard Earth Observing System Chemical Transport Model (GEOS-Chem) is a global three-dimensional (3D) atmospheric transport model widely used to simulate the spatiotemporal variations of atmospheric trace gases, including CO_2 (5, 17, 18). In general, the model accurately simulates large-scale transport of air masses (19, 20), and recent model development has improved mass conservation and tracer advection. The vertical transport of tracers across the planetary boundary layer, however, tends to be weak in northern middle to high latitudes (20, 21). We therefore compared our simulations with vertical profiles taken from aircraft measurements to assess potential biases.

We modified GEOS-Chem v12.0.0 to tag regional CO_2 tracers in order to isolate their contributions to CO_2 variations at individual model grid cells. In this model simulation, CO_2 was treated as a passive tracer that does not affect atmospheric dynamics or drive chemical reactions. Separate regional CO_2 tracers can be tracked independently and eventually summed to define a global response (e.g., refs. 1, 16, 22). In our simulation, each CO_2 tracer reflects surface fluxes from one tagged region.

We defined 13 tagged regions for terrestrial ecosystems (Fig. 1 and *SI Appendix*, Table S1), including three Arctic, four boreal, and two temperate ecosystems. The delineation of these regions was mostly based on plant functional types (PFTs), with the dominant PFT dictating classification as either Arctic or boreal in northern high latitudes. Given the dominance of larch in some parts of Siberia, we further categorized the Siberian boreal region as either deciduous or evergreen (see details in *SI Appendix*, Fig. S1). Although these 13 regions were tagged separately in the transport model, we further grouped them into 6 major regions in the following analyses for clarity. The resulting aggregated regions are high-latitude North America (NH_HighNA), high-latitude Europe (NH_HighEU), high-latitude Siberia (NH_HighSIB), midlatitude temperate ecosystems (NH_Mid), Northern Tropics (NH_Trop), and the Southern Hemisphere (SH) (Fig. 1), with their areas ranging 4.0 to 68.5 $\times$ 10^6 km^2 (*SI Appendix*, Table S1). The transport model was run at 2° in latitude by 2.5° in longitude with 47 vertical levels, driven by hourly meteorological fields from the Modern-Era Retrospective analysis for Research and Application version 2 (MERRA2) reanalysis (23) at a time step of 10 min. Given the data availability of the MERRA2 reanalysis and the prescribed CO_2 fluxes from inversions (see details in the next section), the model was run during 1980 to 2017 with daily outputs following a 3-y cyclic spin-up for 1980.

Prescribed CO_2 Fluxes from Atmospheric Inversions. The land fluxes underlying our GEOS-Chem simulation were derived from two state-of-the-art atmospheric inversion systems constrained by atmospheric CO_2 observations. First, we used monthly land fluxes from the Copernicus Atmosphere Monitoring Service (CAMS) CO_2 global inversion v17r1 (24, 25). CAMSv17r1 covers 1979 to 2017 with a spatial resolution of 1.875° in latitude by 3.75° in longitude. The inversion system (Python VARiational [PyVAR]) assimilates CO_2 flask-air and continuous measurements from up to 111 surface stations in an offline global general circulation model Laboratoire de Météorologie Dynamique version 5A (LMDz5A), with station coverage generally increasing over time (25). Compared to land fluxes from data-driven or process-based LSMs, which have been used for mechanistic attribution of SCA and its changes (1, 4, 7, 10, 16), the inverted fluxes are optimized to reproduce patterns in observed CO_2. However, the optimized fluxes suffer from uncertainties due to transport model errors (26, 27), assignment of prior error statistics, and insufficient data coverage in certain regions, including Siberia and the tropics (*SI Appendix*, Fig. S2*A*, and also see figure 1 in ref. 25).

We also simulated atmospheric CO_2 using monthly land fluxes from CarbonTracker 2017 (CT2017) (28) to better understand the sensitivity of our results to different model formulations. CT2017 only covers the period from 2000 to 2016 (29) but assimilates CO_2 measurements from more surface stations than CAMSv17r1 (*SI Appendix*, Fig. S2), as well as those from aircraft and ship campaigns (254 total sites). In particular, CT2017 assimilates observations from tall towers in Siberia operated by Center for Global Environmental Research, National Institute for Environmental Studies (NIES/CGER) (30, 31). The two inversions also differ in prior flux information, atmospheric transport models, and assimilation techniques (*SI Appendix*, Table S2). Given the shorter time period, model results with CT2017 were used to corroborate those from CAMSv17r1 for 2000 to 2016.

To account for contributions to CO_2 variability from anthropogenic and ocean fluxes, we prescribed monthly fossil fuel emissions from the Carbon Dioxide Information Analysis Center for 1980 to 2013 (32), with emissions for 2013 repeated for 2014 to 2017 and monthly ocean fluxes from CAMSv17r1 for 1980 to 2017.

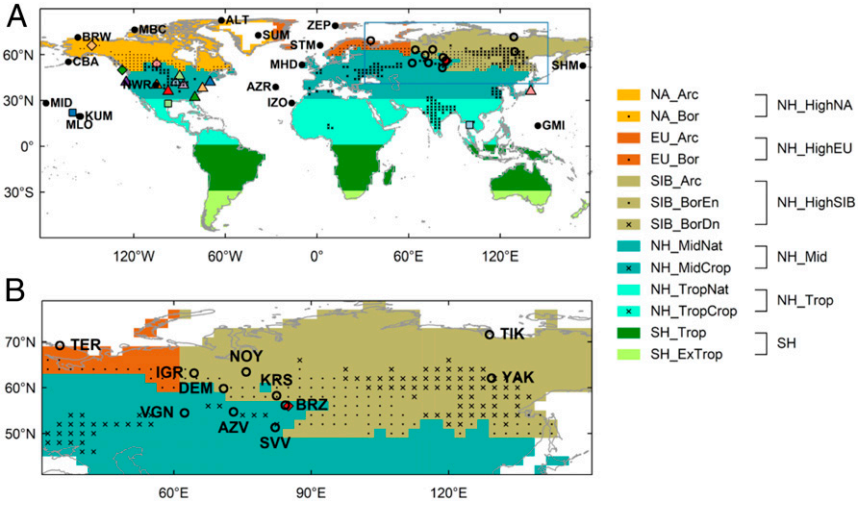

Fig. 1. (*A*) Map of tagged regions and northern surface stations used in this study. Filled circles indicate stations from NOAA's GGGRN assimilated in CAMSv17r1 CO_2 inversion, while open circles indicate Russian stations not assimilated. Colored symbols indicate grid cells where aircraft samples were assembled. (*B*) Close-up map from the blue box in *A*, marking Russian stations.

We note that the transport model that we used for our tagged simulations (i.e., GEOS-Chem) differs from the transport models used in the two atmospheric CO_2 inversions described above (i.e., LMDz for CAMSv17r1 and Tracer Model 5 for CT2017). We therefore evaluated the sensitivity of our results to the choice of transport model by comparing the SCA simulated by GEOS-Chem to that from the CAMSv17r1 or CT2017 posterior simulations (i.e., SCA simulated by LMDz or TM5).

Atmospheric CO_2 Measurements. We conducted site-level comparisons between simulated and observed CO_2 at 16 background stations in the NH and 13 in the SH from National Oceanic and Atmospheric Administration's (NOAA's) Global Greenhouse Gas Reference Network (GGGRN) (33) that were assimilated in CAMSv17r1 (Fig. 1*A* and *SI Appendix*, Fig. S3*A*), each with a record longer than 15 y. We also evaluated model performance at 11 sites not assimilated by CAMSv17r1 in a region with sparse data coverage (Fig. 1*B*), most of which are inland tall towers in Siberia. Detailed information for stations and data sources are provided in *SI Appendix*, Table S3.

We also compared model results to publicly available CO_2 measurements from three aircraft sampling networks and campaigns, including the aircraft program from NOAA's GGGRN (34), the Comprehensive Observation Network for TRace gases by AIrLiner (CONTRAIL) (35, 36), and the NIES/CGER aircraft program (30) (*SI Appendix*, Table S4). To generate a dataset with sufficient spatial and temporal coverage for trend analyses at different vertical levels, we combined all observations from these three networks and grouped them based on GEOS-Chem 2° × 2.5° model grids and 1-km altitude bins between 0 and 8 km (*SI Appendix*, Figs. S4 and S5). We identified 17 grid cells with satisfactory record length (≥10 y) and vertical profiles for model evaluation (Fig. 1*A* and *SI Appendix*, Fig. S4*D*).

Data Processing and Analyses. To isolate the mean annual cycle in simulated and observed CO_2, we applied the CCGvu curve-fitting routine (37). Each time series was decomposed into a quadratic polynomial for the average long-term growth rate and four harmonics for the average seasonal cycle; then the residuals about the function were smoothed using a low-pass filter with 667 and 80 d as long-term and short-term cutoff values and added back to the polynomial and harmonic fit to capture the interannual and short-term variations not determined by the function. We excluded observations outside three SDs of the fit, and in situ continuous measurements were averaged hourly before the curve-fitting procedures. For aircraft measurements at a site, we fitted a curve for each 1-km altitude bin between 0 and 8 km.

At a specific site, the CO_2 SCA over a year was simply calculated as the difference between the annual maximum ($SC_{D_{max}}$) and minimum ($SC_{D_{min}}$) in parts per million (ppm) CO_2 of the detrended curve:

$$SCA = SC_{D_{max}} - SC_{D_{min}}, \quad [1]$$

where D_{max} and D_{min} are the Julian days for the observed or simulated annual CO_2 cycle maximum or minimum. For each tracer i, which reflects surface fluxes from a particular tagged region i, we defined a pseudo maximum ($SC'_{i,D_{max}}$) or minimum ($SC'_{i,D_{min}}$) as the point of its annual cycle corresponding to D_{max} or D_{min}, rather than its actual annual maximum or minimum per se. The pseudo seasonal amplitude of the tracer i, SCA'_i, is then calculated as

$$SCA'_i = SC'_{i,D_{max}} - SC'_{i,D_{min}}. \quad [2]$$

This definition was adopted to account for the phase shift in annual cycles between CO_2 and individual tracers (*SI Appendix*, Fig. S6). The fractional contribution of tracer i to CO_2 SCA, $Frac\_SCA(i)$, was simply the ratio between their mean seasonal amplitudes (i.e., SCA'_i/SCA). The fractional contribution of tracer i to the CO_2 SCA trend, $Frac\_k_{SCA}(i)$, was defined as

$$Frac\_k_{SCA}(i) = k_{SCA'_i} \Big/ k_{SCA} = \Delta SCA'_i / \Delta SCA, \quad [3]$$

where $k_{SCA'_i}$ and k_{SCA} are the trend in the pseudo seasonal amplitude of the tracer i and the trend in CO_2 SCA, and $\Delta SCA'_i$ and ΔSCA indicate changes in seasonal amplitudes over the study period estimated from the respective trend multiplied by data length in years (38 y). We extracted simulated SCA at surface stations as well as aircraft sampling sites for evaluation and attribution. Further, after model evaluation, we conducted pixel-based analyses for the 3D concentration fields to reveal the spatial patterns of trends in SCA and dominant contributors.

We note that the record length and interannual variability (IAV) influence whether a robust trend in SCA can be detected at any individual site. A lack of significant SCA trend in observations or simulations could be due to a short data record and/or large IAV that obscures robust trend detection. To address this, we created a detectability curve to examine how the estimated SCA trend changes with data length. For a given time series of observed or simulated SCA with data length L_0 (in years), we defined a set of moving windows of length $L (10 \le L \le L_0)$. The detectability of a significant trend at window length L was thus calculated as the percentage of moving windows for which a significant SCA trend ($P < 0.05$) was found.

Results

Model Evaluation. Overall, the CO_2 SCA was simulated well by the GEOS-Chem transport model with CAMSv17r1 (Fig. 2*A*). Among the 16 assimilated stations in the NH, there was a strong linear relationship between observed and simulated SCA with a mean bias of 0.1 ± 1.4 ppm (Fig. 2*A* and *SI Appendix*, Fig. S7 and Table S5), which was expected in part because the fluxes are constrained by observations at these sites but not with the same transport model. Model results also agreed well with site observations in the SH (*SI Appendix*, Figs. S3*B* and S8) and compared favorably at nonassimilated stations in Russia with a mean bias of 1.5 ± 3.5 ppm, despite the sparse inland observations assimilated in

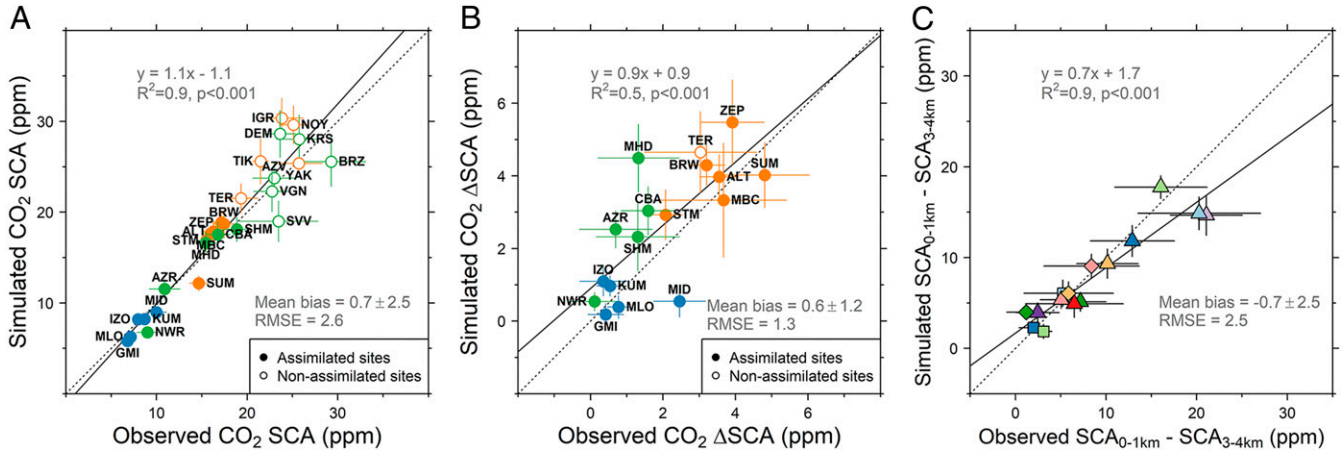

Fig. 2. Evaluation of simulated versus observed (*A*) CO_2 SCA, (*B*) CO_2 ΔSCA, and (*C*) vertical difference in SCA between the altitude bins 0 to 1 km and 3 to 4 km. For *A* and *B*, filled (open) circles represent stations (not) assimilated in the CAMSv17r1 CO_2 inversion. The orange, green, and blue circles indicate high-latitude (60 to 90 °N), midlatitude (30 to 60 °N), and low-latitude (0 to 30 °N) stations. Dotted and solid lines represent the unit line and least squares regression line, respectively. The colored symbols in *C* correspond to those in Fig. 1*A*. Error bars denote ±1σ.

CAMSv17r1 in this region (*SI Appendix*, Fig. S2*A* and Table S5 and also see figure 1 in ref. 25). In fact, this bias was actually smaller than that obtained when using CT2017 fluxes, which assimilated some of these data (Fig. 2*A* and *SI Appendix*, Fig. S9). Compared to the posterior fields from CAMSv17r1 (LMDz) and CT2017 (TM5), the SCA simulated from GEOS-Chem showed a small bias of +10% on average for stations at middle to high latitudes (*SI Appendix*, Fig. S10). The overestimation of SCA for low-altitude stations and underestimation for high-altitude stations (Summit and Niwot Ridge in *SI Appendix*, Fig. S10) in GEOS-Chem reflects weaker vertical mixing compared to LMDz and TM5 in the northern extratropics, as already noted in refs. 20, 21. However, as the model bias in vertical mixing is zonally symmetric in GEOS-Chem (21), it likely does not have differential impact on the tagged regions across a given latitude band.

The model also reasonably reproduced the north–south pattern in SCA trends, including at the nonassimilated Teriberka site in western Russia (Fig. 2*B* and *SI Appendix*, Fig. S7). Again, the general overestimation of trends at most middle- to high-latitude sites may be due to the fact that the rather weak vertical transport in the northern extratropics by GEOS-Chem (20, 21) can trap the surface fluxes within the boundary layer where air masses are sampled, amplifying the SCA increase. Given the sensitivity of SCA to vertical mixing, we demonstrate that the model generally captured the vertical difference in SCA between the altitude bins 0 to 1 km and 3 to 4 km at 17 aircraft sites (Fig. 2*C*), as well as the vertical profiles of the CO_2 seasonal phasing (*SI Appendix*, Figs. S11–S15). The SCA, trends, and vertical profiles simulated from CAMSv17r1 also corroborate well those from CT2017 (*SI Appendix*, Figs. S7, S8, and S11–S15), which assimilated more observations, including those from Siberian tall towers (*SI Appendix*, Fig. S2*B*). Together, these results suggest that the GEOS-Chem simulations can satisfactorily reproduce SCA, its trend, and its vertical profiles at observation sites with only small bias in the trend at surface locations.

Regional Contributions to Site-Level SCA and Its Trend. Arctic-boreal and temperate ecosystems each contributed roughly 50% to the climatological mean SCA at high-latitude (60 to 90 °N) and midlatitude sites (30 to 60 °N) (Fig. 3*A*), with overall larger amplitude at high-latitude sites (16.4 ± 2.5 ppm vs. 13.0 ± 4.1 ppm). Given the large size differences among tagged regions (*SI Appendix*, Table S1), the contribution from temperate ecosystems was much smaller when normalized by area (Fig. 3*B* and *SI Appendix*, Fig. S16*A*). Among the Arctic-boreal ecosystems, the contributions from North America (NH_HighNA) and Siberia (NH_HighSIB) were roughly equal across high-latitude and midlatitude sites, whether or not area is taken into account (Fig. 3*A* and *SI Appendix*, Fig. S16*A* and Table S6). Note that regional contributions varied across sites within each latitude band (*SI Appendix*, Fig. S17). Model results from CT2017 generally agreed with those from CAMSv17r1 over 2000 to 2016, except that a greater contribution of SCA was attributed to NH_HighSIB (~30%) than NH_HighNA (<20%) in both high latitudes and midlatitudes (*SI Appendix*, Fig. S18 and Table S7).

Although NH_HighNA and NH_HighSIB contributed similarly to the mean high-latitude SCA, the SCA trend originated largely from NH_HighSIB (Fig. 3*C*). Across high-latitude sites, the increase in SCA over 1980 to 2017 (ΔSCA) was 3.8 ± 0.4 ppm, and the contribution from NH_HighSIB was 1.6 ± 0.3 ppm versus 0.5 ± 0.4 ppm from NH_HighNA. The contribution from NH_HighNA was highly variable across high-latitude sites (*SI Appendix*, Fig. S19), with the largest signal detected at Utqiagvik (Barrow; 1.1 ± 0.3 ppm) in response to the significant increase in the NEE seasonal amplitude (SCA_{NEE}) over interior Alaska and some parts of Canada (*SI Appendix*, Fig. S20*A*). In contrast, the contribution from NH_HighSIB was on average much larger and more uniform across sites (*SI Appendix*, Fig. S19), as most of the high-latitude sites examined here are remotely influenced by long-range transport of the well-mixed Siberian air masses with a strong increase in SCA_{NEE} (Fig. 3*D* and *SI Appendix*, Fig. S20*A*). Temperate ecosystems also contributed 1.5 ± 0.3 ppm (~40%) to ΔSCA at high-latitude sites. For midlatitude sites, ΔSCA was dominated by changes in NH_HighSIB and NH_Mid, which contributed 1.1 ± 0.5 ppm (61.4 ± 36.5%) and 0.9 ± 0.6 ppm (31.8 ± 21.9%), respectively (Fig. 3*C* and *SI Appendix*, Table S8). Notably, when normalized by geographic area, the contribution from NH_HighSIB to ΔSCA stands out, equivalent to more than three times that from NH_Mid for middle- to high-latitude sites (Fig. 3*D* and *SI Appendix*, Fig. S16*B*), despite the similar magnitudes of their integrated contributions (Fig. 3*C*). For low-latitude sites, ΔSCA increased due to flux changes in NH_Mid and NH_HighSIB, with offset from NH_Trop (Fig. 3*C* and *SI Appendix*, Table S8).

Regional Contributions to Large-Scale Patterns of ΔSCA. Although long-term observations are only available from a discrete network of sites, we used the model results to explore global patterns of ΔSCA (Fig. 4). As expected from site-level analyses, the simulations showed that the seasonal cycle of atmospheric CO_2 amplified across much of the NH north of 30°N. At the surface, the largest increases occurred in the circumpolar regions of North America and eastern Siberia at high latitudes, as well as the eastern United States and the Black Sea region in Eurasia. There are also regions where no trends or negative trends were found, for example, in Mongolia and the subtropics (Fig. 4*A*). At higher altitudes, these spatial features are still relatively consistent, although with smaller magnitudes (Fig. 4 *D* and *G*).

The spatial drivers of ΔSCA differ both regionally and by altitude (Fig. 4 *B*, *E*, and *H*). NH_HighSIB was the dominant contributor to ΔSCA for 64% of high-latitude areas at the surface, with most of the remainder dominated by fluxes in NH_Mid (31%). NH_HighNA was the dominant contributor for only 5% of surface high-latitude areas (*SI Appendix*, Table S9), and its influence is limited to eastern Alaska and northwestern Canada. Zonal analyses confirmed that NH_HighSIB played a dominant role in driving large-scale surface ΔSCA in high latitudes, on average contributing 2.1 ± 1.0 ppm of 4.1 ± 0.9 ppm (Fig. 4*C* and *SI Appendix*, Table S10). At the surface midlatitudes and throughout the midtroposphere of the middle to high latitudes, the contribution from NH_Mid to ΔSCA became more important, with NH_Mid emerging as the dominant contributor for 70 to 100% of area (*SI Appendix*, Table S9). However, the contribution from NH_HighSIB was still significant, with a fractional contribution to ΔSCA as high as 30 to 40% (*SI Appendix*, Table S10).

Despite the apparent large-scale amplification in the free troposphere (Fig. 4 *D* and *G*), observations from aircraft profiles generally did not show statistically significant trends in SCA, as the short record length and large IAV prevented robust detection of trends (Fig. 5 *B–D* and *SI Appendix*, Figs. S21 and S22). One exception was the high-latitude aircraft profiles in Alaska (Fig. 5*A*), where a (marginally) robust increase in SCA was found between 2 and 6 km and was generally captured by simulations. Based on simulated CO_2 at aircraft sites, we showed that at least ~15 y of data are required to achieve ≥50% detectability of significant SCA trends (Fig. 5 *E–H* and *SI Appendix*, Fig. S23 and also see *Materials and Methods* for details). For certain altitude levels at some sites (e.g., 2 to 4 km in Hawaii; Fig. 5*H*), the detectability of a robust SCA trend remains well below 50% even when the assumed record length approaches 30 y, suggesting that strong IAV obscures detection of a decadal trend.

Discussion

Our study illustrates the distribution of SCA trends and the contributions from different regions using a tagged CO_2 transport model and observationally constrained fluxes. Results showed that

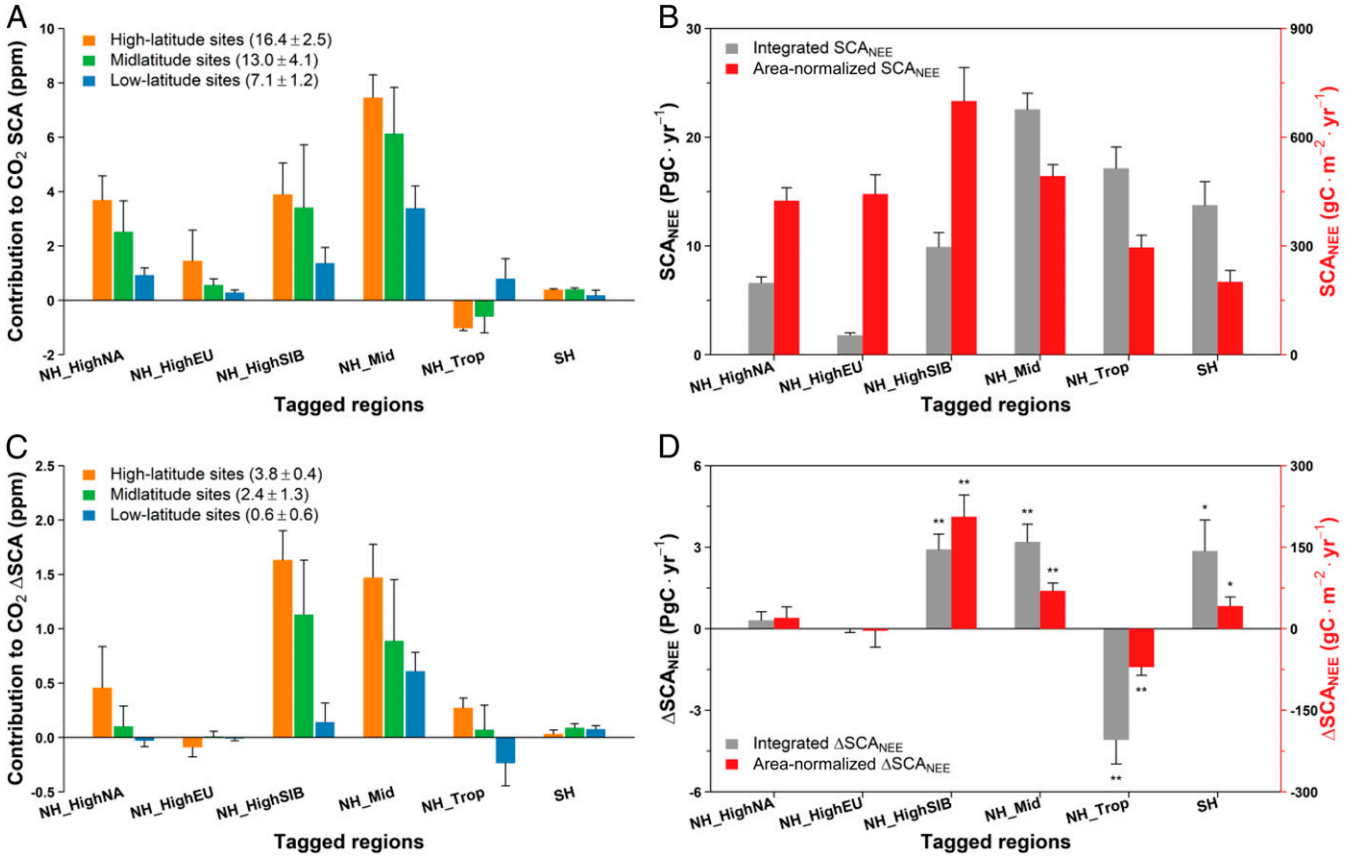

Fig. 3. (*A* and *C*) Contribution of the six major tagged regions to site-level CO_2 SCA and ΔSCA in relation to (*B* and *D*) their NEE seasonal amplitudes (SCA_{NEE}) and changes (ΔSCA_{NEE}). For *A* and *C*, the orange, green, and blue bars represent flux imprints from different tagged regions on *x* axis for northern high-latitude (60 to 90 °N; $n = 7$), midlatitude (30 to 60 °N; $n = 5$), and low-latitude (0 to 30 °N; $n = 5$) stations, respectively, with the numbers in the parentheses showing the mean SCA or ΔSCA averaged within station groups. Only the 16 stations from NOAA's GGGRN and the nonassimilated station Teriberka in Russia are included. For *B* and *D*, the gray and red bars represent the integrated and area-normalized SCA_{NEE} or ΔSCA_{NEE} for different tagged regions. Analyses were based on NEE from the CAMSv17r1 inversion for 1980 to 2017.

Siberian and temperate ecosystems together shape the overall atmospheric CO_2 seasonal amplification in the NH and confirm the importance of northern extratropical land ecosystems in driving the observed amplitude trend (2–4). Particularly, at northern high latitudes in the lower troposphere, Siberian boreal forests and tundra dominate the trend in SCA, whereas impacts from Arctic-boreal North America are much smaller and geographically localized. At northern surface midlatitudes and throughout the midtroposphere, the dominant contributor is temperate ecosystems, but Siberia still plays a significant role.

It should be noted that CAMSv17r1 did not directly assimilate data from all atmospheric CO_2 observation stations in Siberia, calling into question the reliability of the large increasing trend in NEE seasonality that drives the CO_2 amplification in this region. We note, however, that the spatial footprint of marine boundary layer stations in northern high latitudes, particularly, Utqiagvik (Barrow), Alert, Cold Bay, and Shemya Island (*SI Appendix*, Fig. S2*A*), encompasses fluxes in northern and eastern Siberia (*SI Appendix*, Fig. S24, and also see refs. 38–42). Further, we used a Monte Carlo method to estimate uncertainties of the posterior fluxes for NH_HighSIB between the time periods 2013 to 2017 and 1980 to 1984 (43, 44), which indicated that the seasonal flux estimates during the peak growing season do not overlap at the one-sigma level for the two time periods (*SI Appendix*, Fig. S20*B*). This robustness is confirmed by the good fit of our CAMSv17r1-driven simulation against measurements from the unassimilated Siberian sites (*SI Appendix*, Fig. S9), as well as the agreement with results from the simulation driven by CT2017 that assimilated these sites (*SI Appendix*, Figs. S7, S8, and S11–S15). Therefore, despite the uncertainty inherent in constraining fluxes in this undersampled region, the increasing seasonal carbon exchange over the entire NH_HighSIB is statistically significant, and the seasonal amplitude increase reflects enhanced net summer carbon uptake.

The strong high-latitude imprints on CO_2 seasonal amplification identified using our top-down approach corroborate observations of ecological changes and confirm that these changes scale up to impart substantial trends on large-scale carbon cycle dynamics within the region. At northern high latitudes, various field and remote-sensing–based studies have shown a greening trend and northward shrub expansion over the past several decades (13, 45–47). Greening has been attributed to diverse causes, including the impact of warming on growing season length, active layer depth over vast areas of permafrost, and water and nutrient availability (48, 49). Changes in atmospheric composition via, e.g., CO_2 fertilization may also increase the magnitude of growing season productivity (8, 9). These changes likely lead to enhanced summer carbon uptake and a deeper CO_2 minimum (1, 2, 4, 50). Site-level flux measurements and regional-scale synthesis have also revealed increased wintertime carbon release over Arctic tundra in response to warming (51–55), with increased CO_2 buildup outside the growing season. Together, these ecological changes have resulted in a substantial and

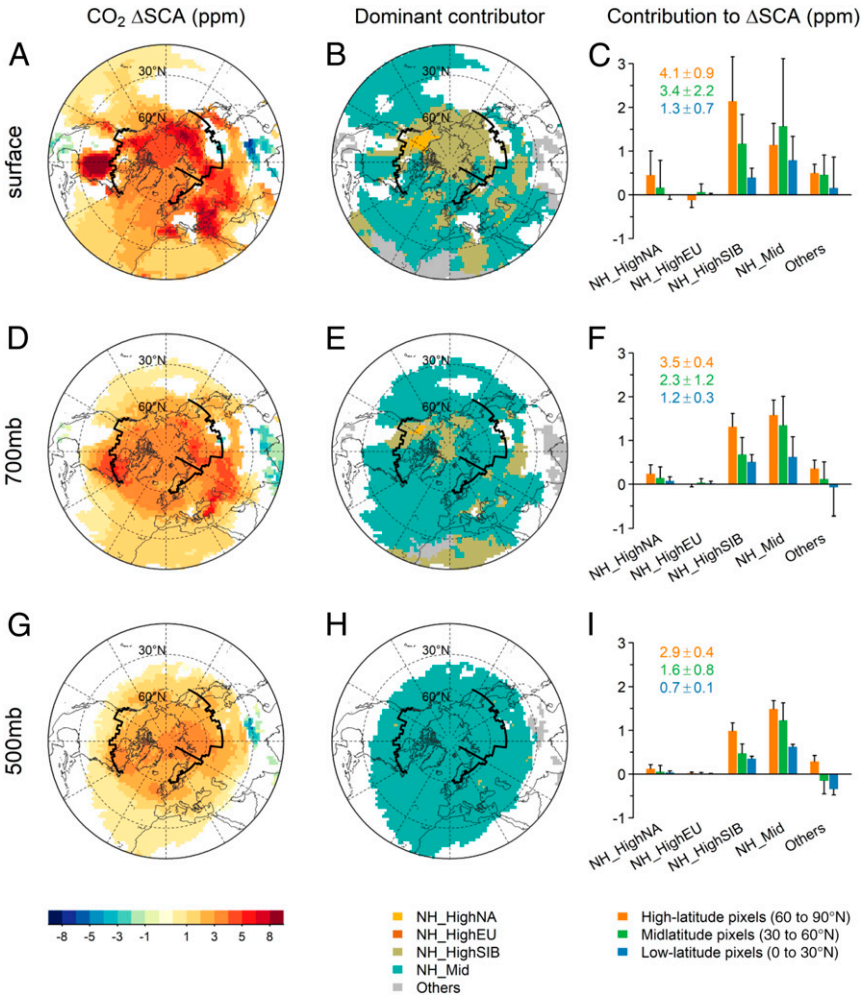

Fig. 4. Spatial patterns of CO_2 ΔSCA and their dominant driving region in the NH. (*A*, *D*, and *G*) ΔSCA at the surface, 700 mb, and 500 mb calculated from model results with CAMSv17r1 for 1980 to 2017. Only pixels with significant trends ($P < 0.05$) are shaded. (*B*, *E*, and *H*) Maps of the dominant contributor to ΔSCA. For each pixel, this is the tagged region that imparts the largest ΔSCA. (*C*, *F*, and *I*) Zonal analyses of the regional contributions to ΔSCA. The orange, green, and blue bars represent flux imprints from different tagged regions on the *x* axis for northern high-latitude (60 to 90 °N), midlatitude (30 to 60 °N), and low-latitude (0 to 30 °N) pixels, respectively. The numbers on the top left show the mean ΔSCA averaged over each latitude band. Only pixels with significant positive trends (i.e., ΔSCA > 0, $P < 0.05$) were analyzed. The bold black lines delineate the three high-latitude tagged regions, i.e., NH_HighNA, NH_HighEU, and NH_HighSIB.

sustained increase in the seasonal net exchange of CO_2 in northern high latitudes.

Our results also confirm divergent ecological responses between Siberia and high-latitude North America to the changes in climate and atmospheric forcings. Pervasive vegetation greening has been observed in Siberia, with the exception of some parts of western Siberia (48, 56). In contrast, although greening has been observed over Arctic-boreal North America, the region has experienced a larger proportion of browning trends (13, 14, 57). Browning has been spatially correlated with climate-related disturbances, including intensified fire regimes (58–60), biotic infestations (61–63), and resulting tree mortality (64–67). Climate variations in this region can also directly affect ecosystem fluxes via warming-induced drought stress (68–70). As a result, earlier springs tend to be associated with drier conditions later in the growing season and lead to decreases in summer productivity (49, 71, 72). Differences in seasonal amplification between these two continents may also carry over to longer timescales: CAMSv17r1 shows a growing carbon sink in Siberia over the past 4 decades, while the carbon balance in Arctic-boreal North America does not exhibit a significant trend (*SI Appendix*, Table S11). Together, the contrasts between the two continents suggest that the long-standing positive relationships between temperature and carbon cycling have declined or even reversed, particularly in high-latitude North America (38, 57, 73–75). The change in this relationship may be due, in part, to the increased temperature sensitivity of respiration compared to that of productivity. A recent study based on long-term CO_2 observations at Utqiagvik (Barrow) suggested that the turnover rate of carbon cycling in Arctic North America has increased (76), which may render more carbon vulnerable to the impact of climate change in the long term.

In addition to providing direct regional attribution of CO_2 seasonal amplification, our results on the differential contributions from Siberia and Arctic-boreal North America may offer insight into the mechanistic drivers. Current state-of-the-art LSMs disagree on the role of climate change in regulating the SCA increase over northern high latitudes (7–10, 12). This is in contrast to CO_2 fertilization, which has been identified as the primary driver of amplification in high latitudes based on results from an ensemble of LSMs (8–10, 12). Depending on region-specific patterns of changes in climate and ecosystem responses, the climate effects on seasonal carbon exchange could add to or offset the overall positive effects of CO_2 fertilization. The divergent patterns

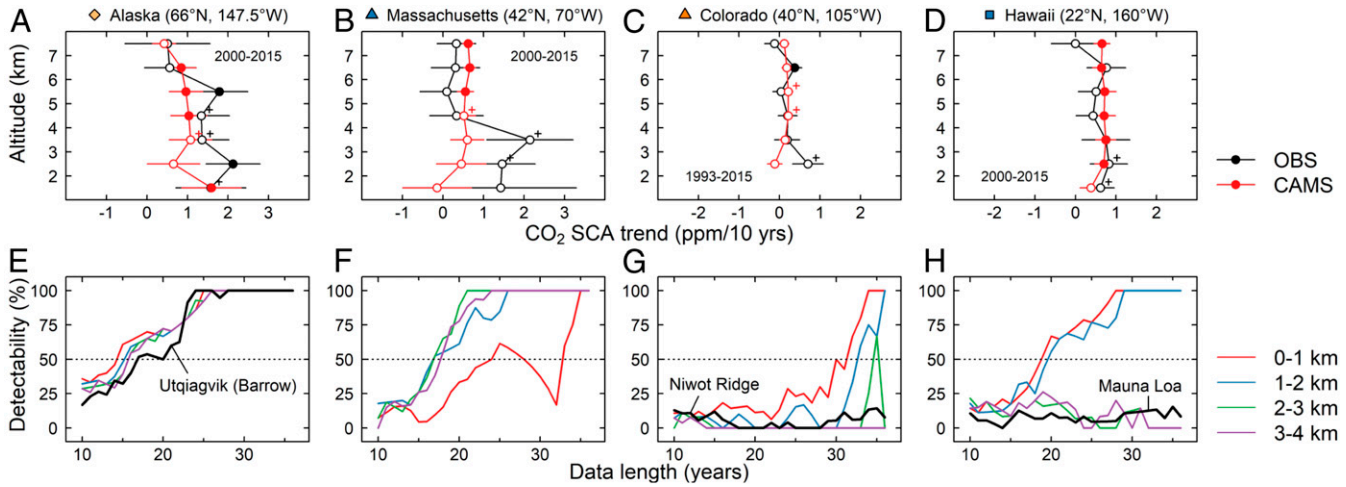

Fig. 5. The trends in CO_2 SCA for aircraft profiles at four sites. (*A–D*) Comparison of simulated versus observed SCA trends for altitude bins between 1 and 8 km from aircraft profiles in Alaska (*A*), Massachusetts (*B*), Colorado (*C*), and Hawaii (*D*). Filled circles represent significant trends ($P < 0.05$), whereas open circles with pluses represent marginally significant trends ($P < 0.1$). Error bars show $\pm 1\sigma$. (*E–H*) Significance of the SCA trend as a function of data record length based on model results at each site (see details in *Materials and Methods*). The point of intersection between each curve and the horizontal dotted line represents the minimal data length required to achieve ≥50% detectability of a significant trend. For *E*, *G*, and *H*, the black lines represent the detectability curves for observations from the background stations Utqiagvik (Barrow; 11 m asl), Niwot Ridge (3,523 m asl), and Mauna Loa (3,399 m asl), which are in good agreement with model results at corresponding altitude levels.

between Arctic-boreal North America and Siberia from our top-down approach provide independent atmospheric constraints on high-latitude ecosystem process modeling in response to these global change drivers. That some models do not capture the contrasting patterns between the two continents calls for improvement of LSMs to better characterize regional properties and processes associated with the divergent ecosystem responses (77).

Our results also highlight the importance of midlatitude processes in driving CO_2 seasonal amplification in the NH, even though the per-area contribution from temperate ecosystems is small compared to that from Siberia (Fig. 3*D* and *SI Appendix*, Fig. S16*B*). Previous studies showed that the simulated amplitude increase driven by land fluxes from LSMs is generally underestimated in the midtroposphere and that matching the observed amplitude trend would not be possible by solely adjusting high-latitude land fluxes (3, 6). The inability of LSMs to account for temperate flux seasonality trends could be due to inaccurate parameterization of CO_2 fertilization and climate sensitivity (78–80), as well as underrepresentation of processes and interactions such as nutrient cycling and land management (8–11). In our study, the largest CO_2 amplitude increase at the surface of midlatitudes is found over the central and eastern United States and southeastern Europe (Fig. 4*A* and *SI Appendix*, Fig. S20*A*), downwind of the regions where agriculture, managed forests, and forests recovering from historical disturbance occur (81–84). The geographical patterns may suggest agriculture intensification and land cover change as important drivers of the increase in temperate flux seasonality, but their roles remain under debate (8, 10–12, 82). An improved understanding requires a detailed characterization of land use and land cover change, as well as better representation of agricultural management and forest demography in LSMs (11, 85).

It may also be possible to separate the imprint of middle- and high-latitude flux changes by considering differences in amplification at the surface and in the midtroposphere (Fig. 4). The predominance of temperate ecosystems in driving midtropospheric SCA trends confirms the importance of accounting for the spatial imprint of atmospheric transport on patterns of atmospheric CO_2 (5). We note, however, that in contrast with model results displaying a widespread SCA increase in the free troposphere (Fig. 4 *D* and *G*), observations from aircraft do not show significant trends except for a site in Alaska (Fig. 5*A*). While discrete ground observational networks dating back to 1960s have provided valuable datasets for diagnosing changes in CO_2 seasonal cycles (2, 3, 86), the relatively short records of aircraft measurements (usually <15 y) prevent robust detection of trends. As efforts have been made to deploy new observations to underobserved regions, it remains important to maintain and expand current ground networks and aircraft profiles for long-term monitoring of changes in atmospheric CO_2 and carbon balance (87).

Data Availability. The CO_2 tracer concentration fields simulated from the tagged transport model GEOS-Chem v12.0.0 are available at the University of Michigan Library Deep Blue online repository (88). The CO_2 inversion products CAMSv17r1 and CT2017 are publicly available, with data sources presented in *SI Appendix*, Table S2. The ground-based atmospheric CO_2 measurements from NOAA's GGGRN and tall towers in Siberia are publicly available, with data sources presented in *SI Appendix*, Table S3. The atmospheric CO_2 measurements from the three aircraft platforms NOAA's GGGRN, CONTRAIL, and NIES/CGER are publicly available, with data sources presented in *SI Appendix*, Table S4.

ACKNOWLEDGMENTS. This study was funded by a NASA Carbon Cycle Science and Arctic-Boreal Vulnerability Experiment (ABoVE) grant (NNX17AE13G) to X.L., G.K.-A., and B.M.R., as well as a NASA ABoVE grant (NNX17AC61A) to C.S. M.S. acknowledges financial support by the Global Environmental Research Coordination System from Ministry of the Environment of Japan. We thank data providers of two CO_2 inversion products: CAMS version 17r1 from European Centre for Medium-Range Weather Forecast and CarbonTracker CT2017 provided by NOAA's Global Monitoring Laboratory, Boulder, CO. We are grateful to the GEOS-Chem model development group and the HYbrid Single-Particle Lagrangian Integrated Trajectory (HYSPLIT) development group. We also thank L. Birch for valuable discussions. This research was supported in part through computational resources and services provided by Advanced Research Computing at the University of Michigan, Ann Arbor.

1. J. T. Randerson, M. V. Thompson, T. J. Conway, I. Y. Fung, C. B. Field, The contribution of terrestrial sources and sinks to trends in the seasonal cycle of atmospheric carbon dioxide. *Global Biogeochem. Cycles* **11**, 535–560 (1997).
2. C. D. Keeling, J. F. S. Chin, T. P. Whorf, Increased activity of northern vegetation inferred from atmospheric CO_2 measurements. *Nature* **382**, 146–149 (1996).
3. H. D. Graven *et al*., Enhanced seasonal exchange of CO_2 by northern ecosystems since 1960. *Science* **341**, 1085–1089 (2013).
4. J. T. Randerson, C. B. Field, I. Y. Fung, P. P. Tans, Increases in early season ecosystem uptake explain recent changes in the seasonal cycle of atmospheric CO_2 at high northern latitudes. *Geophys. Res. Lett.* **26**, 2765–2768 (1999).
5. E. A. Barnes, N. Parazoo, C. Orbe, A. S. Denning, Isentropic transport and the seasonal cycle amplitude of CO_2. *J. Geophys. Res.* **121**, 8106–8124 (2016).
6. R. T. Thomas *et al*., Increased light-use efficiency in northern terrestrial ecosystems indicated by CO_2 and greening observations. *Geophys. Res. Lett.* **43**, 11,339-11,349 (2016).
7. M. Forkel *et al*., Enhanced seasonal CO_2 exchange caused by amplified plant productivity in northern ecosystems. *Science* **351**, 696–699 (2016).
8. F. Zhao *et al*., Role of CO_2, climate and land use in regulating the seasonal amplitude increase of carbon fluxes in terrestrial ecosystems: A multimodel analysis. *Biogeosciences* **13**, 5121–5137 (2016).
9. A. Ito *et al*., Decadal trends in the seasonal-cycle amplitude of terrestrial CO_2 exchange resulting from the ensemble of terrestrial biosphere models. *Tellus B* **68**, 28968 (2016).
10. S. Piao *et al*., On the causes of trends in the seasonal amplitude of atmospheric CO_2. *Glob. Change Biol.* **24**, 608–616 (2018).
11. N. Zeng *et al*., Agricultural Green Revolution as a driver of increasing atmospheric CO_2 seasonal amplitude. *Nature* **515**, 394–397 (2014).
12. A. Bastos *et al*., Contrasting effects of CO_2 fertilization, land-use change and warming on seasonal amplitude of Northern Hemisphere CO_2 exchange. *Atmos. Chem. Phys.* **19**, 12361–12375 (2019).
13. K. C. Guay *et al*., Vegetation productivity patterns at high northern latitudes: A multi-sensor satellite data assessment. *Glob. Change Biol.* **20**, 3147–3158 (2014).
14. J. Ju, J. G. Masek, The vegetation greenness trend in Canada and US Alaska from 1984–2012 Landsat data. *Remote Sens. Environ.* **176**, 1–16 (2016).
15. M. P. Girardin *et al*., No growth stimulation of Canada's boreal forest under half-century of combined warming and CO_2 fertilization. *Proc. Natl. Acad. Sci. U.S.A.* **113**, E8406–E8414 (2016).
16. C. D. Nevison *et al*., Contribution of ocean, fossil fuel, land biosphere, and biomass burning carbon fluxes to seasonal and interannual variability in atmospheric CO_2. *J. Geophys. Res.* **113**, G01010 (2008).
17. R. Nassar *et al*., Modeling global atmospheric CO_2 with improved emission inventories and CO_2 production from the oxidation of other carbon species. *Geosci. Model Dev.* **3**, 689–716 (2010).
18. G. Keppel-Aleks *et al*., Separating the influence of temperature, drought, and fire on interannual variability in atmospheric CO_2. *Global Biogeochem. Cycles* **28**, 1295–1310 (2014).
19. P. K. Patra *et al*., TransCom model simulations of CH_4 and related species: Linking transport, surface flux and chemical loss with CH_4 variability in the troposphere and lower stratosphere. *Atmos. Chem. Phys.* **11**, 12813–12837 (2011).
20. S. C. Wofsy; HIPPO Science Team and Cooperating Modellers and Satellite Teams, HIAPER Pole-to-Pole Observations (HIPPO): Fine-grained, global-scale measurements of climatically important atmospheric gases and aerosols. *Philos. Trans. A Math. Phys. Eng. Sci.* **369**, 2073–2086 (2011).
21. A. E. Schuh *et al*., Quantifying the impact of atmospheric transport uncertainty on CO_2 surface flux estimates. *Global Biogeochem. Cycles* **33**, 484–500 (2019).
22. J. Liptak, G. Keppel-Aleks, K. Lindsay, Drivers of multi-century trends in the atmospheric CO_2 mean annual cycle in a prognostic ESM. *Biogeosciences* **14**, 1383–1401 (2017).
23. R. Gelaro *et al*., The modern-era retrospective analysis for research and applications, version 2 (MERRA-2). *J. Clim.* **30**, 5419–5454 (2017).
24. F. Chevallier, Description of the CO_2 inversion production chain. https://atmosphere.copernicus.eu/sites/default/files/FileRepository/Resources/Documentation/Fluxes/CAMS73_2015SC1_D73.1.3_201603_CO2_Inversion_Production_Chain.pdf. Accessed 16 February 2019.
25. F. Chevallier, Validation report for the inverted CO_2 fluxes, v17r1. https://atmosphere.copernicus.eu/sites/default/files/2018-10/CAMS73_2015SC3_D73.1.4.2-1979-2017-v1_201807_v1-1.pdf. Accessed 21 November 2018.
26. K. R. Gurney *et al*., Towards robust regional estimates of CO_2 sources and sinks using atmospheric transport models. *Nature* **415**, 626–630 (2002).
27. S. Basu *et al*., The impact of transport model differences on CO_2 surface flux estimates from OCO-2 retrievals of column average CO_2. *Atmos. Chem. Phys.* **18**, 7189–7215 (2018).
28. W. Peters *et al*., An atmospheric perspective on North American carbon dioxide exchange: CarbonTracker. *Proc. Natl. Acad. Sci. U.S.A.* **104**, 18925–18930 (2007).
29. CarbonTracker Team, CarbonTracker Documentation (CT2017 release) (2018). https://www.esrl.noaa.gov/gmd/ccgg/carbontracker/CT2017/. Accessed 20 March 2019.
30. M. Sasakawa *et al*., Aircraft and tower measurements of CO_2 concentration in the planetary boundary layer and the lower free troposphere over southern taiga in West Siberia: Long-term records from 2002 to 2011. *J. Geophys. Res.* **118**, 9489–9498 (2013).
31. M. Sasakawa *et al*., Continuous measurements of methane from a tower network over Siberia. *Tellus B Chem. Phys. Meterol.* **62**, 403–416 (2010).
32. R. J. Andres, T. A. Boden, Data from "Monthly fossil-fuel CO_2 emissions: Uncertainty of emissions gridded by one degree latitude by one degree longitude (Uncertainties, V.2016)." ESS-DIVE Data Archive. https://doi.org/10.3334/CDIAC/FFE.MONTHLYUNCERTAINTY.2016. Accessed 1 September 2018.
33. E. J. Dlugokencky *et al*, Data from "Atmospheric carbon dioxide dry air mole fractions from the NOAA GML Carbon Cycle Cooperative Global Air Sampling Network, 1968-2017." ESRL Global Monitoring Laboratory. ftp://aftp.cmdl.noaa.gov/data/trace_gases/co2/flask/surface/. Accessed 23 November 2018.
34. C. Sweeney *et al*, Data from "NOAA carbon cycle and greenhouse gases group aircraft-based measurements of CO_2, CH_4, CO, N_2O, H_2 and SF_6 in flask-air samples taken since 1992." NOAA National Centers for Environmental Information. http://dx.doi.org/10.7289/V5N58JMF. Accessed 7 January 2019.
35. T. Machida *et al*., Worldwide measurements of atmospheric CO_2 and other trace gas species using commercial airlines. *J. Atmos. Ocean. Technol.* **25**, 1744–1754 (2008).
36. T. Machida, K. Ishijima, Y. Niwa, K. Tsuboi, Y. Sawa, H. Matsueda, Data from "Atmospheric CO_2 mole fraction data of CONTRAIL-CME, Version 2017.1.0." National Institute for Environmental Studies, Japan. https://doi.org/10.17595/20180208.001. Accessed 19 January 2019.
37. K. W. Thoning, P. P. Tans, W. D. Komhyr, Atmospheric carbon dioxide at Mauna Loa Observatory: 2. Analysis of the NOAA GMCC data, 1974–1985. *J. Geophys. Res.* **94**, 8549–8565 (1989).
38. S. Piao *et al*., Weakening temperature control on the interannual variations of spring carbon uptake across northern lands. *Nat. Clim. Chang.* **7**, 359–363 (2017).
39. A. Berchet *et al*., Atmospheric constraints on the methane emissions from the East Siberian shelf. *Atmos. Chem. Phys.* **16**, 4147–4157 (2016).
40. T. Kaminski, R. Giering, M. Heimann, Sensitivity of the seasonal cycle of CO_2 at remote monitoring stations with respect to seasonal surface exchange fluxes determined with the adjoint of an atmospheric transport model. *Phys. Chem. Earth* **21**, 457–462 (1996).
41. S. Murayama, S. Taguchi, K. Higuchi, Interannual variation in the atmospheric CO_2 growth rate: Role of atmospheric transport in the Northern Hemisphere. *J. Geophys. Res.* **109**, D02305 (2004).
42. P. Peylin *et al*., A 3-dimensional study of $\delta^{18}O$ in atmospheric CO_2: Contribution of different land ecosystems. *Tellus B Chem. Phys. Meterol.* **51**, 642–667 (1999).
43. F. Chevallier, F.-M. Bréon, P. J. Rayner, Contribution of the Orbiting Carbon Observatory to the estimation of CO_2 sources and sinks: Theoretical study in a variational data assimilation framework. *J. Geophys. Res.* **112**, D09307 (2007).
44. F. Chevallier, C. W. O'Dell, Error statistics of Bayesian CO_2 flux inversion schemes as seen from GOSAT. *Geophys. Res. Lett.* **40**, 1252–1256 (2013).
45. S. C. Elmendorf *et al*., Plot-scale evidence of tundra vegetation change and links to recent summer warming. *Nat. Clim. Chang.* **2**, 453–457 (2012).
46. I. H. Myers-Smith *et al*., Climate sensitivity of shrub growth across the tundra biome. *Nat. Clim. Chang.* **5**, 887–891 (2015).
47. Z. Zhu *et al*., Greening of the Earth and its drivers. *Nat. Clim. Chang.* **6**, 791–795 (2016).
48. T. Park *et al*., Changes in growing season duration and productivity of northern vegetation inferred from long-term remote sensing data. *Environ. Res. Lett.* **11**, 084001 (2016).
49. J. Barichivich *et al*., Temperature and snow-mediated moisture controls of summer photosynthetic activity in Northern terrestrial ecosystems between 1982 and 2011. *Remote Sens.* **6**, 1390–1431 (2014).
50. L. R. Welp *et al*., Increasing summer net CO_2 uptake in high northern ecosystems inferred from atmospheric inversions and comparisons to remote-sensing NDVI. *Atmos. Chem. Phys.* **16**, 9047–9066 (2016).
51. W. C. Oechel *et al*., Recent change of Arctic tundra ecosystems from a net carbon dioxide sink to a source. *Nature* **361**, 520–523 (1993).
52. R. Commane *et al*., Carbon dioxide sources from Alaska driven by increasing early winter respiration from Arctic tundra. *Proc. Natl. Acad. Sci. U.S.A.* **114**, 5361–5366 (2017).
53. E. F. Belshe, E. A. G. Schuur, B. M. Bolker, Tundra ecosystems observed to be CO_2 sources due to differential amplification of the carbon cycle. *Ecol. Lett.* **16**, 1307–1315 (2013).
54. E. S. Euskirchen, M. S. Bret-Harte, G. R. Shaver, C. W. Edgar, V. E. Romanovsky, Long-term release of carbon dioxide from Arctic tundra ecosystems in Alaska. *Ecosystems* **20**, 960–974 (2017).
55. S. M. Natali *et al*., Large loss of CO_2 in winter observed across the northern permafrost region. *Nat. Clim. Chang.* **9**, 852–857 (2019).
56. W. Buermann *et al*., Recent shift in Eurasian boreal forest greening response may be associated with warmer and drier summers. *Geophys. Res. Lett.* **41**, 1995–2002 (2014).
57. J. Bi *et al*., Divergent Arctic-boreal vegetation changes between North America and Eurasia over the past 30 years. *Remote Sens.* **5**, 2093–2112 (2013).
58. S. J. Goetz, A. G. Bunn, G. J. Fiske, R. A. Houghton, Satellite-observed photosynthetic trends across boreal North America associated with climate and fire disturbance. *Proc. Natl. Acad. Sci. U.S.A.* **102**, 13521–13525 (2005).
59. E. S. Kasischke *et al*., Alaska's changing fire regime—Implications for the vulnerability of its boreal forests. *Can. J. Res.* **40**, 1313–1324 (2010).
60. S. Veraverbeke *et al*., Lightning as a major driver of recent large fire years in North American boreal forests. *Nat. Clim. Chang.* **7**, 529–534 (2017).
61. J. A. Hicke *et al*., Effects of biotic disturbances on forest carbon cycling in the United States and Canada. *Glob. Change Biol.* **18**, 7–34 (2012).
62. B. J. Bentz *et al*., Climate change and bark beetles of the western United States and Canada: Direct and indirect effects. *Bioscience* **60**, 602–613 (2010).
63. D. S. Pureswaran *et al*., Climate-induced changes in host tree–insect phenology may drive ecological state-shift in boreal forests. *Ecology* **96**, 1480–1491 (2015).
64. M. Michaelian, E. H. Hogg, R. J. Hall, E. Arsenault, Massive mortality of aspen following severe drought along the southern edge of the Canadian boreal forest. *Glob. Change Biol.* **17**, 2084–2094 (2011).
65. C. Peng *et al*., A drought-induced pervasive increase in tree mortality across Canada's boreal forests. *Nat. Clim. Chang.* **1**, 467–471 (2011).

66. Y. Luo, H. Y. H. Chen, Climate change-associated tree mortality increases without decreasing water availability. *Ecol. Lett.* **18**, 1207–1215 (2015).
67. B. M. Rogers *et al*., Detecting early warning signals of tree mortality in boreal North America using multiscale satellite data. *Glob. Change Biol.* **24**, 2284–2304 (2018).
68. X. J. Walker, M. C. Mack, J. F. Johnstone, Stable carbon isotope analysis reveals widespread drought stress in boreal black spruce forests. *Glob. Change Biol.* **21**, 3102–3113 (2015).
69. M. P. Girardin *et al*., Negative impacts of high temperatures on growth of black spruce forests intensify with the anticipated climate warming. *Glob. Change Biol.* **22**, 627–643 (2016).
70. R. A. Hember, W. A. Kurz, N. C. Coops, Relationships between individual-tree mortality and water-balance variables indicate positive trends in water stress-induced tree mortality across North America. *Glob. Change Biol.* **23**, 1691–1710 (2017).
71. B. R. Parida, W. Buermann, Increasing summer drying in North American ecosystems in response to longer nonfrozen periods. *Geophys. Res. Lett.* **41**, 5476–5483 (2014).
72. W. Buermann, P. R. Bikash, M. Jung, D. H. Burn, M. Reichstein, Earlier springs decrease peak summer productivity in North American boreal forests. *Environ. Res. Lett.* **8**, 024027 (2013).
73. V. A. Barber, G. P. Juday, B. P. Finney, Reduced growth of Alaskan white spruce in the twentieth century from temperature-induced drought stress. *Nature* **405**, 668–673 (2000).
74. A. H. Lloyd, A. G. Bunn, Responses of the circumpolar boreal forest to 20th century climate variability. *Environ. Res. Lett.* **2**, 045013 (2007).
75. P. Zhu *et al*., Recent warming has resulted in smaller gains in net carbon uptake in northern high latitudes. *J. Clim.* **32**, 5849–5863 (2019).
76. S.-J. Jeong *et al*., Accelerating rates of Arctic carbon cycling revealed by long-term atmospheric CO_2 measurements. *Sci. Adv.* **4**, eaao1167 (2018).
77. B. M. Rogers, A. J. Soja, M. L. Goulden, J. T. Randerson, Influence of tree species on continental differences in boreal fires and climate feedbacks. *Nat. Geosci.* **8**, 228–234 (2015).
78. D. Schimel, B. B. Stephens, J. B. Fisher, Effect of increasing CO_2 on the terrestrial carbon cycle. *Proc. Natl. Acad. Sci. U.S.A.* **112**, 436–441 (2015).
79. W. Kolby Smith *et al*., Large divergence of satellite and Earth system model estimates of global terrestrial CO_2 fertilization. *Nat. Clim. Chang.* **6**, 306–310 (2016).
80. C. R. Rollinson *et al*., Emergent climate and CO_2 sensitivities of net primary productivity in ecosystem models do not agree with empirical data in temperate forests of eastern North America. *Glob. Change Biol.* **23**, 2755–2767 (2017).
81. M. Albani, D. Medvigy, G. C. Hurtt, P. R. Moorcroft, The contributions of land-use change, CO_2 fertilization, and climate variability to the Eastern US carbon sink. *Glob. Change Biol.* **12**, 2370–2390 (2006).
82. J. M. Gray *et al*., Direct human influence on atmospheric CO_2 seasonality from increased cropland productivity. *Nature* **515**, 398–401 (2014).
83. R. Buitenwerf, B. Sandel, S. Normand, A. Mimet, J.-C. Svenning, Land surface greening suggests vigorous woody regrowth throughout European semi-natural vegetation. *Glob. Change Biol.* **24**, 5789–5801 (2018).
84. M. Kondo *et al*., Plant regrowth as a driver of recent enhancement of terrestrial CO_2 uptake. *Geophys. Res. Lett.* **45**, 4820–4830 (2018).
85. T. A. M. Pugh *et al*., Role of forest regrowth in global carbon sink dynamics. *Proc. Natl. Acad. Sci. U.S.A.* **116**, 4382–4387 (2019).
86. W. Buermann *et al*., The changing carbon cycle at Mauna Loa Observatory. *Proc. Natl. Acad. Sci. U.S.A.* **104**, 4249–4254 (2007).
87. N. C. Parazoo *et al*., Detecting regional patterns of changing CO_2 flux in Alaska. *Proc. Natl. Acad. Sci. U.S.A.* **113**, 7733–7738 (2016).
88. X. Lin, G. Keppel-Aleks, B. Rogers, L. Birch, Simulated CO_2 tracer concentrations in the Northern Hemisphere from a tagged transport model GEOS-Chem v12.0.0 [dataset]. University of Michigan Library Deep Blue. https://doi.org/10.7302/rp59-rw535. Deposited 16 April 2020.